scientific reports

OPEN

Molecular dynamics analysis of subsurface brittleness mechanism of nanocrystalline 3C-SiC rough friction surface

Xiang Ning[1,3,4], Jiawen Huang[2,4], Rumeng Zhang[1,3,4], Dongliang Liu[1,3], Jiao Li[1,3] & Nanxing Wu[1,3✉]

To study the effect of polycrystalline 3C-SiC rough friction surface on the mechanism of subsurface brittleness during nanocrystalline grinding. Initial grinding models of polycrystalline 3C-SiC and diamond abrasive grains on rough friction surfaces are developed using molecular dynamics methods and the Voronoi method for constructing polycrystalline abrasive grains. The processing mechanism of 3C-SiC is analyzed by post-processing methods such as dislocation defect analysis, atomic arrangement analysis and stress analysis. At 2.6 *nm*, "stress concentration" occurs between the abrasive particles and the workpiece, forming irregular force shapes. The larger the grain size, the smaller the crystal hardness, the greater the possibility of crystal fracture, and it is obvious in the crystal of larger grains. At 8 nm, the crystal breaks and creates vacancies. The roughness of the polycrystalline 3C-SiC friction surface and the cross-cutting mechanism between grains with grain boundaries are found to be effective in ameliorating the damage in the subsurface layer.

3C-SiC has excellent properties such as good natural sphericity and self-sharpening, excellent creep resistance and fracture resistance, good sintering activity, and large gap width[1–3]. It is widely used in aerospace precision fields such as high temperature, high pressure, and high magnetic field. However, the high hardness and brittleness of 3C-SiC make it highly susceptible to major forms of machining damage such as cracks, pitting and lines during machining[4–6]. These damages increase the likelihood of various defects or fractures in 3C-SiC materials during service. This greatly limits the development and application of 3C-SiC in the field of nano-precision. The application of nano-grinding is conducive to the further development of 3C-SiC materials. The removal, grinding and polishing of 3C-SiC materials by nano-machining technology make the application prospect of 3C-SiC materials more targeted and extensive. However, there are significant differences between nano-grinding and conventional grinding in terms of material removal methods and brittleness mechanisms[7–11]. Under the operational requirements of nanoscale precision nano-grinding, it is difficult to control the range and depth of material processing and material shaping during nano-grinding. The grinding process often produces a series of special physical phenomena such as micro-wear and size effect[12–15].

The application of molecular dynamics method to simulate the nano-milling process of polycrystalline 3C-SiC materials allows real-time tracking and observation of the deformation, dislocation generation, stacking, transformations, or other changes of the specimen under loading. Tian et al.[16] studied the nano-mechanical properties of sic under the action of nano-indentation and nano-crack, and selected the C and Si surfaces of 4H-SiC and 6H-SiC for nano-grinding through molecular dynamics. The results showed the 4H-SiC displaying greater normal resistance than 6H-SiC, C surfaces may be easier to machine than Si surfaces. Goel et al.[17] explored the mechanical properties and defect generation process of nanoscale SiC. The sp3-sp2 structural transition in nano-scale SiC occurring during nano-cutting was found to be related to non-hydrostatic stress conditions

[1]School of Mechanical and Electronic Engineering, Jingdezhen Ceramic University, Jingdezhen 333403, Jiangxi, China. [2]School of Mechanical and Electronic Engineering, Jingdezhen University, Jingdezhen 333400, Jiangxi, China. [3]National Engineering Research Center for Domestic & Building Ceramics, Jingdezhen 333403, Jiangxi, China. [4]These authors contributed equally: Xiang Ning, Jiawen Huang and Rumeng Zhang. ✉email: jelfptocm_wnx@163.com

through simulation studies. The introduction of non-hydrostatic stress conditions can lead to the formation of structures similar to SiC nano-tubes. Li et al.[18] studied the grinding machinability of 3D C/ C-sic composites, and conducted grinding experiments of 3D C/ C-SiC composites with resin bonded diamond grinding wheel. The results indicated that the fracture of C/C-SiC composites was mainly brittle fracture. Liu et al.[19] studied the surface/subsurface damage mechanism caused by cracks in grinding SiC ceramics, and used smooth particle fluid mechanics to simulate the grinding mechanism in SiC grinding process, including the influence of material removal process and scratch speed on crack growth. As a result, the material removal process went through pure ductile cutting mode, tough-brittle transition and pure brittle cutting mode as the depth of cut increased. The above research is helpful for us to study the surface and subsurface brittleness machining mechanism of SiC nano-grinding, the simulation analysis of two single crystal isomeric SiC(4H-SiC, 6H-SiC) and different surfaces. However, there is a lack of research on nanoscale polycrystalline SiC as well as rough friction surfaces, the effect of cutting force on the grinding process of rough surfaces of nano-polycrystalline SiC needs further investigation[20] Therefore, The variation of material removal rate during nano-crystal milling is studied. The brittle mechanisms of the surface and subsurface of the rough friction surface material of polycrystalline 3C-SiC during nano-grinding are analyzed.

Methods
Determine the experimental simulation scheme of rough friction surface polycrystalline 3C-SiC nano-grinding

The molecular dynamics-based Voronoi method analyses the material removal process of polycrystalline 3C-SiC rough surfaces machined under the action of diamond abrasive grains[21–23]. The interaction field between polycrystalline 3C-SiC and diamond is established by modifying the Tessoff-Vashista coupling potential function to improve the calculation of the interatomic interaction potential. Characteristics of typical families, microtypical ensembles are analysed to construct relaxation polymorphic conversion equations, optimise the relaxation energy conversion process, shorten the thermodynamic dynamic equilibrium time. On the basis of the diversity of parameters of the Voronoi method, a system integral calculation method combining pressure, displacement and atomic velocity is proposed, thus improving the defect of a single calculation parameter. The influence of trace parameters on the integration results is avoided, fulfilling the completeness of the calculation principle of atomic systems. The 3C-SiC processing and forming process together with the post-processing methods such as dislocation defect analysis, atomic arrangement analysis and stress analysis are analysed. Explore pure ductility modes, for brittle-assisted ductility modes an brittle modes during the material removal phase[24–26]. Molecular dynamics simulation is a simulation method using computer technology to implement material properties. Experimental modelling of polycrystalline 3C-SiC nano-friction with rough friction surfaces is carried out by molecular dynamics simulation. The experimental model of polycrystalline 3C-SiC nano-lithography with rough friction surface is established by molecular dynamics simulation. The whole simulation experiment is divided into four main parts. The first part is to determine the relevant parameters in the initial environmental process, such as time step, atom type and boundary conditions, and to establish the initial loading conditions for the simulation experiment. The second part refers to the establishment of sinusoidal rough friction surfaces during the modelling process, as well as the determination of the dimensions of the polycrystalline 3C-SiC workpiece, and the dimensions and positions of the diamond abrasive grains. The third part is the relaxation process, it makes the whole system reach thermodynamic equilibrium and eliminates the internal stresses may be generated before grinding. The steady state of the relaxation process directly affects the state of the grinding process. The fourth part is the most important grinding process.

$$Z = A \times Sin\left(x \times b \times \frac{\pi}{T_1}\right) \times Sin\left(y \times c \times \frac{\pi}{T_1}\right) \tag{1}$$

Equation (1) is the expression formula of the sinusoidal friction surface. A represents the amplitude of the surface; x and y represent the distance from the X and Y axes; b and c determine the speed of the fluctuation of the surface; $T1$ and $T2$ represent the period of the fluctuation from the X and Y axes respectively.

The correlation between the force results and the surface morphology as well as the crystal behaviour is established with the following equations:

$$\begin{cases} F_{ductile} = \left(a + b\ln\left(\frac{V_s}{l y \varepsilon 0}\right)\right)\frac{2}{3} \cdot \frac{H}{2.8}\left[2 + \ln\left(\frac{E \cdot \frac{H}{2.8} \cdot \tan\beta + 4(1-2\nu)}{6 \cdot (1-\nu)}\right)\right] \cdot n \cdot \theta 1 \cdot R \cdot \theta 2 \cdot r \\ F_{brittle} = (5 + 5 \cdot rand())\left(a + b\ln\left(\frac{V_s}{l y \varepsilon 0}\right)\right)\frac{2}{3} \cdot \frac{H}{2.8}\left[2 + \ln\left(\frac{E \cdot \frac{H}{2.8} \cdot \tan\beta + 4(1-2\nu)}{6 \cdot (1-\nu)}\right)\right] \cdot n \cdot \theta 1 \cdot R \cdot \theta 2 \cdot r \end{cases} \tag{2}$$

where, H is the hardness, β is the abrasive grit inclination, ν is the Poisson's ratio, rand() indicates the value is between 0 and 1. R and r are the radius of the large arc and small arc respectively, $\theta 1$ and $\theta 2$ are the corresponding circular angle of the large arc and small arc respectively, $F_{ductile}$ and $F_{brittle}$ are the grinding force for ductile removal and brittle removal modes respectively[27,28].

Table 1 lists the parameters associated with the polycrystalline 3C-SiC silicon nano-grinding model. These include the size of the workpiece, the number of atoms associated between the workpiece and the abrasive, the selected family, the time step and the grinding temperature. In molecular dynamics simulation, ensemble determines the relationship between system and environment. In the relaxation process, the canonical series (NVT) is applied, the number, volume, and temperature of particles in the system under this ensemble are determined, and only heat exchange occurs, with the total energy fixed. The microcanonical ensemble (NVE) is applied during processing with the energy state at thermodynamic equilibrium reached by relaxation set as the initial

The relevant parameter	Parameter values
Workpiece size	10.435 nm × 10.435 nm × 10.43 5 nm
Workpiece atomic number	102,753
Height of conical diamond indenter	2 nm
Number of diamond indenter atoms	1846
Diamond lattice constant	a = 3.56 Å
3C-SiC lattice constant	a = 4.259 Å
Ensemble selection	NVT, NVE
Creasing temperature	300K
Timestep	1 fs

Table 1. Model parameter table.

state. In the machining simulation process, the system energy is restored to the energy steady state in a gradient increase and decrease mode[29–31].

Establishment of rough friction surface polycrystalline 3C-SiC nano-grinding model

Figure 1 shows the experimental model of rough friction surface polycrystalline 3C-SiC nano-grinding. In order to better introduce the setting of the model, the rough surface map, high cloud map, layering map and polycrystal map are used to represent it. The length, width and height of the workpiece are 10.435 nm. The front end of the abrasive particle is a semi-cylinder with a diameter of 2 nm and a length of 3 nm. The back end is a cuboid with a length of 3 nm, a width of 1 nm and a height of 2 nm. At the top of the workpiece is the surface of sine curve with a height of 1 nm. Figure 1A shows the top view of the friction surface and the image generated by layered coloring according to the height of the Z-axis direction. As shown in Fig. 1C, a boundary layer with a thickness of 1 nm is set at the bottom and the left side of the workpiece to maintain the stability of the polycrystalline 3C-SiC workpiece during the grinding process. To eliminate the heat generated in the grinding process between abrasive particles and polycrystalline 3C-SiC sic workpiece, a 1 nm thermostatic layer is set on the basis of the boundary layer. Therefore, the main processing area is the area outside the boundary layer and the thermostatic layer, namely the Newton layer. As shown in Fig. 1D, for the polycrystalline morphology of the model, the crystal
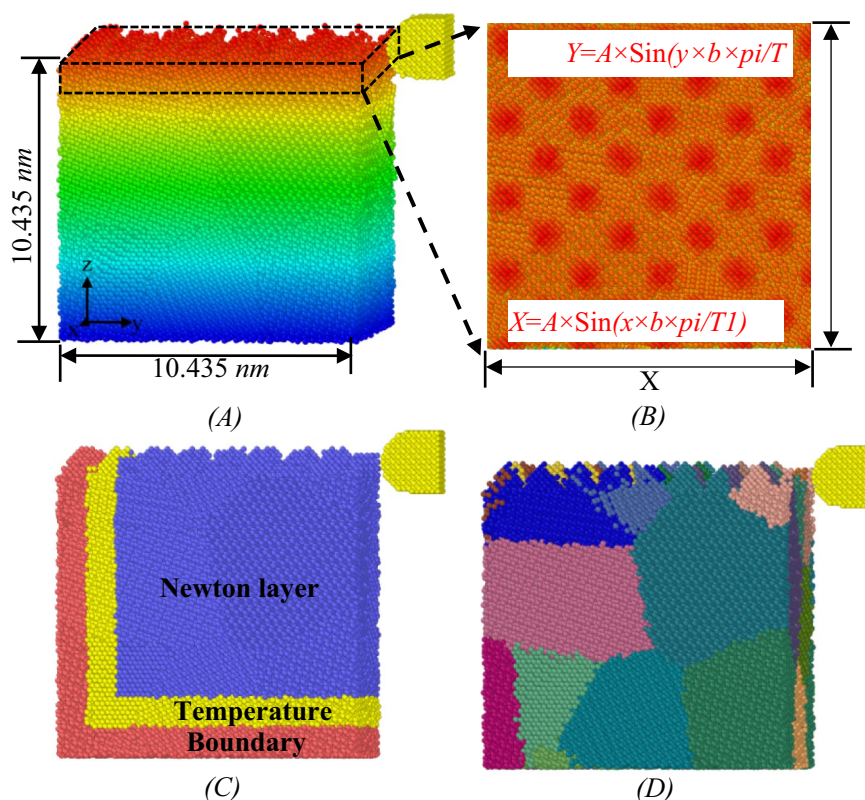

Figure 1. Model diagram of polycrystalline 3C-SiC rough surface.

arrangement and structure inside the workpiece are identified by means of Polyhedral template matching and post-processing of Grain segmentation.

Numerical solution of MD model
Potential function and related calculation principle

Figure 2 shows the flow chart of molecular dynamics model establishment. The modeling process is mainly divided into three main bodies, namely, the model of the initial position of the polycrystalline 3C-SiC friction surface workpiece and diamond abrasive grains, the process of thermodynamic dynamic equilibrium between the polycrystalline 3C-SiC friction surface workpiece and diamond abrasive grains, and the grinding process between the polycrystalline 3C-SiC friction surface workpiece and diamond abrasive grains. The first body is to establish the 3C-SiC particle structure, and build the workpiece and friction surface model, fill the 3C-SiC particles into the model, forming the initial model of polycrystalline 3C-SiC friction surface workpiece; The second part is to calculate the position and velocity between atoms under the construction of the Tersoff-Vashishta coupling potential function, and then reach the thermodynamic steady state after thermodynamic relaxation. The third main body is the polycrystalline 3C-SiC friction surface workpiece and diamond abrasive under regular and microregular ensemble. Calculate the force field caused by the interaction between atoms and the position and velocity of the atoms after the interaction, collect and output the related physical quantities, such as the force force, displacement, velocity, temperature, etc.

During polycrystalline silicon carbide nanocrystal milling, the interatomic interaction mechanism between silicon carbide and diamond is complex. It is necessary to consider the C–Si, C–C, and Si–Si bonds within silicon carbide, as well as the C–C bonds within diamond, the C–C and Si–C bond interactions between silicon carbide and diamond. The Tersoff potential function is mainly used in the cutting simulation of SIC materials, the Vashishta potential function is mainly used in the simulation of nano-indentation. Combining these two potentials, the simulation of polycrystalline SIC nano-grinding is carried out. Tersoff potential function[32] and Vashishta potential function[33] are commonly used in polycrystalline silicon carbide. The Tersoff potential function is mainly used for cutting simulations of SiC materials, the Vashishta potential function is mainly used for nanoindentation simulations of SiC, with Crystalline 3C-SiC being a type of silicon carbide. Therefore, these two potential functions are also used for grinding simulation.

The Tersoff-Vashishta potential function is expressed as follows:

$$E = \frac{1}{4} \sum_i \sum_{j \neq i} \left(1 - \sin \frac{\pi(r_{ij} + \delta - R)}{2D} \right) \left[f_R(r_{ij} + \delta) + b_{ij} f_A(r_{ij} + \delta) \right] \tag{3}$$
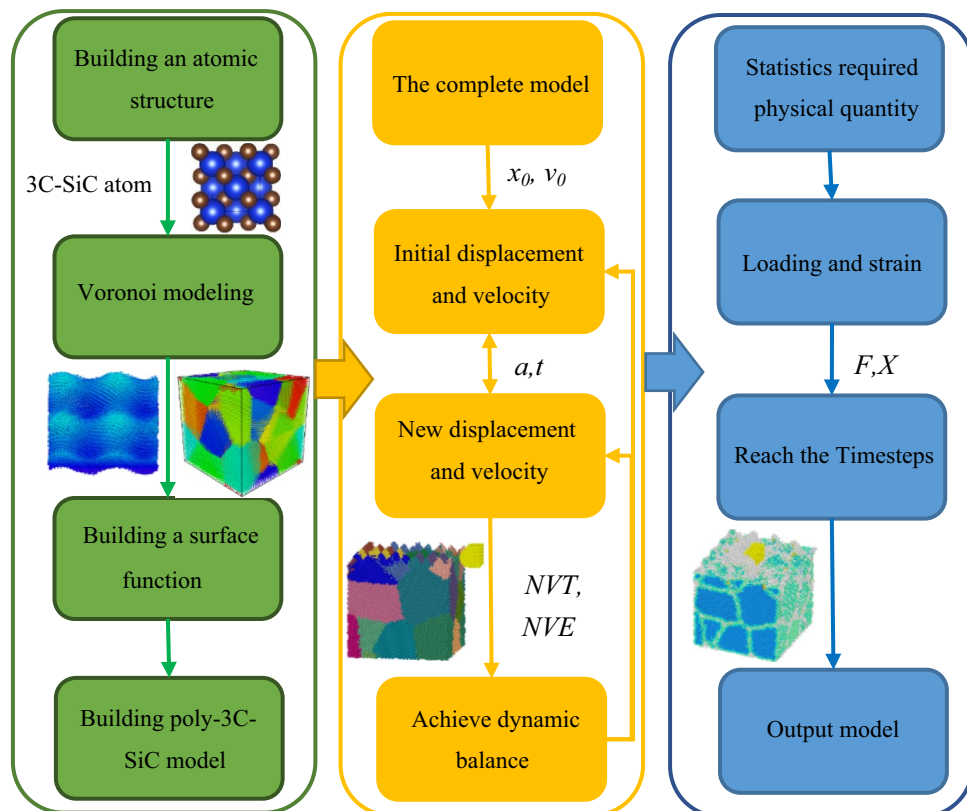

Figure 2. Flow chart of molecular dynamics model establishment.

$$U = \sum_{i}^{N} \sum_{j>i}^{N} U_{ij}^{(2)}(r_{ij}) + \sum_{i}^{N} \sum_{j \neq i}^{N} \sum_{k>j,k \neq i}^{N} U_{ijk}^{(3)}(r_{ij}, r_{ik}, \theta_{ijk}) \tag{4}$$

$$U_{ij}^{(2)}(r) = \frac{H_{ij}}{r^{\eta ij}} + \frac{Z_i Z_j}{r} \exp(-r/\lambda_{1,ij}) - \frac{Dij}{r^4} \exp(-r/\lambda_{4,ij}) - \frac{Wij}{r^6}, r < r_{c,ij} \tag{5}$$

$$U_{ijk}^{(3)}(r_{ij}, r_{ik}, \theta_{ijk}) = B_{ijk} \frac{[\cos\theta_{ijk} - \cos\theta_{0ijk}]^2}{1 + C_{ijk}[\cos\theta_{0ijk}]^2} \times exp\left(\frac{r_{ij}}{rij - r_{0,ij}}\right) \exp\left(\frac{r_{ik}}{r_{ik} - r_{0,ik}}\right) \tag{6}$$

f_R is the repulsive function, the interaction force of two-body terms; f_A is the attraction function, and the three-body interaction force; U is the total potential of the atomic system, and $U^{(2)}$ is the two-body term action potential. $U^{(3)}$ is the action potential of the three-body term. The sum of the two-body term is always the sum of all adjacent j atoms within the truncation distance, and the two-body term moves and tilts by a linear function so that the energy and force are zero at. The sum of the three-body terms is always the sum of all adjacent atoms i and k within the truncation distance, where the exponential screening function becomes zero.

Relaxation polymorphic transition equation
The molecular dynamics simulation method assumes all atoms move in a way adhering to the motion theorems of classical Newtonian mechanics. According to the second theorem of motion of classical Newtonian mechanics, the force $F_i(t)$ on the *ith* atom at time *t*:

$$F_i(t) = m_i \frac{d^2}{dt^2} r_i(t) \tag{7}$$

m_i is the mass of the first atom, $v_i(t)$ is the speed of the ith atom at time t, $r_i(t)$ is the position of the ith atom at time t. Newton's equation of motion describes the trajectory of the atom. By integrating the time, the speed and position of the atom at any time can be determined after the initial speed and position of the system are given. In order to improve the solving efficiency of Newton's equation of motion, the Verlet algorithm is modified. The Verity-Verlet algorithm can simultaneously obtain the position, Velocity and acceleration of each atom at the same time. The specific solution is as follows:

$$v_i(t + \delta t) = v_i(t) + \frac{1}{2}\left[\frac{d^2}{dt^2} r_i(t + \delta t) + \frac{d^2}{dt^2} r_i(t)\right]\delta t \tag{8}$$

δt is a small quantity called the time step. The Velocity-Verlet algorithm not only ensures the accuracy of the algorithm, but also reduces the amount of computation. Thus, calculations with large time steps can be performed. Relaxation multiple steady state transition equation:

$$W = (N + 1)k_B T_t P_d^2 \tag{9}$$

where N is the number of atoms, k_B is the Boltzmann constant, and T_t is the target temperature of the pressure regulator (Martyna). If a thermostat is defined, T_t is the target temperature for the thermostat. If no thermostat is defined, T_t is set to the current temperature of the system at the time of initializing the barometric regulator. If this temperature is too low, the simulation will exit with an error.

Results and discussion
Elastoplastic deformation of polycrystalline silicon carbide nano-grinding
Figure 3 shows the elastic–plastic analysis diagram in the grinding process of polycrystalline 3C-SiC rough friction surface. Figure 3a shows the stress of workpiece at different positions in the grinding process, and Fig. 3a shows the local magnification diagram at 0–2 *nm* position in Fig. 3a. From Fig. 3a, we can see the force on the workpiece in Y direction and Z direction increases, while the force along the X-axis remains relatively low, fluctuating around 25 *nN*. When the abrasive feeding reaches about 2.2 *nm*, the force on the Y direction increases gently, while the force on the Z direction still increases in a wavy way but with a small upward trend. The force on the workpiece is increasing at the beginning of the grinding process, and the trend of the force in the Y-direction and Z-direction is basically the same. Tensile simulations are carried out at several grinding points in the model, identifying the point of elastic–plastic deformation at the polycrystalline 3C-SiC grinding depth close to 0.8 nm. At 0–0.8 *nm*, the workpiece is in the elastic deformation stage, the force in all directions is small and changes in the same way. Figure 3b shows the line graph of cutting elastic strain at 1.8 *nm* position when the elastic stress range is 0–0.1 *nN*. It is clearly seen the elastic stresses generated inside the polycrystalline 3C-SiC workpiece during the rough friction surface stage of diamond grit grinding of polycrystalline 3C-SiC. These elastic stresses are mainly distributed in the abrasive grains. With the cutting action of abrasive grains, plastic deformation occurs first near the abrasive grains and at the grain boundaries. Because the dispersed conduction force at the grain boundaries protects the interior of the grains, there is a tendency of elastic deformation to plastic deformation of the grains, but no plastic deformation occurs. Figure 3b₁ shows the grinding trace after the removal of abrasive grains, and the trace generated by the grinding of abrasive grains is shown on the right. On the left is the main force part of the abrasive grain feed movement. It is observed that the force portion is located in the direction of the feed motion and at the bottom of the abrasive grain. The force exerted
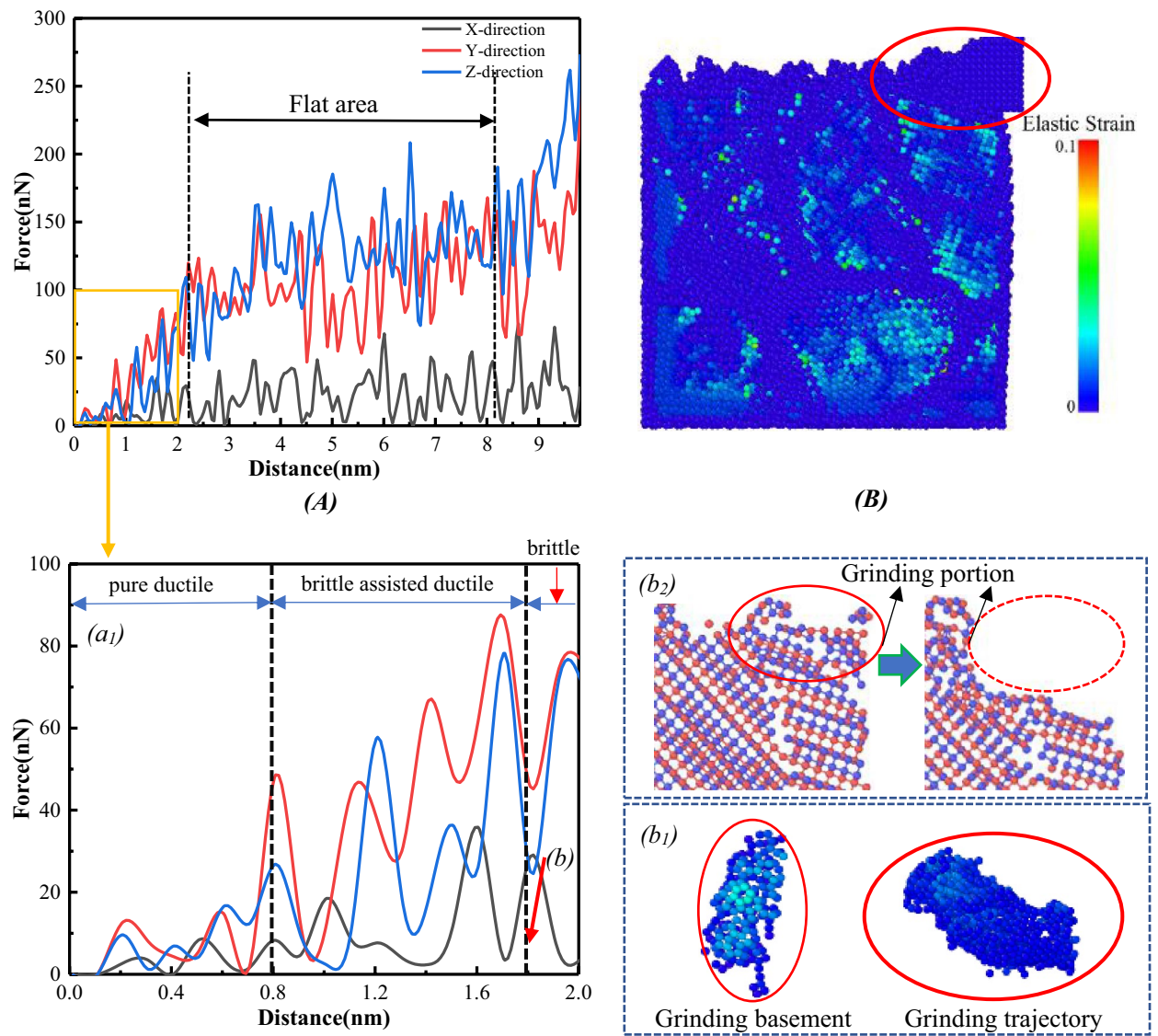
Figure 3. Analysis of elastic–plastic deformation of polycrystalline 3C-SiC rough surface by cutting.

by the abrasive on the workpiece is mainly at the contact between the abrasive and the workpiece. Figure 3b$_2$ is a schematic diagram of the arrangement of atoms in the grinding process of abrasive grains. Under the action of diamond abrasive grains, the covalent bonds of silicon carbide atoms are broken and displaced, the atoms are stacked forward in the shape of abrasive grains. The order of arrangement between the atoms is disturbed, the atomic bonds are reconnected, resulting in the formation of vacancies and other defects. Diamond abrasives mainly break the atomic bonds during the grinding process, causing the relative slip between the atoms, thereby rebuilding the atomic structure.

Stress analysis of polycrystalline silicon carbide nano-grinding

Figure 4 shows the cutting stress nemo-grams of the polycrystalline 3C-SiC rough friction surface at different positions. Figure 4a shows the top view of the abrasive grinding to the position of 2 *nm*, and the cutting stress range is 0-1nN. Figure 4a$_1$ shows the top view of the abrasive when it is ground to the 2 nm position with a cutting stress range of 0–1 nN. An accumulation of red atoms can be seen directly in front of the abrasive grain, indicating the area in front of the grain is most affected. Force conduction is also present on the upper surface of the friction, but it is relatively small in the vicinity of the abrasive grain. In order to observe the images in the vicinity of diamond abrasive grains, images of abrasive grains after grinding in the top view direction are produced by enlarging the abrasive grains grinding map *(a$_2$)* and the abrasive marks image *(a$_3$)*. The stress wave generated on the ground surface increases with the friction distance, and the cross-sectional direction changes significantly. Figure 4b shows the stress cloud map for grinding up to 2.6 nm and the stress trace map of the particles near the abrasive grains. In Fig. 4b$_1$, the rough friction surface of polycrystalline 3C-SiC exhibits a concave orientation pattern in the presence of diamond abrasive grains. Due to the irregular shape of the cutting surface, the forces move differently. As the depth of grinding deepens, it can be noticed the stress distribution is
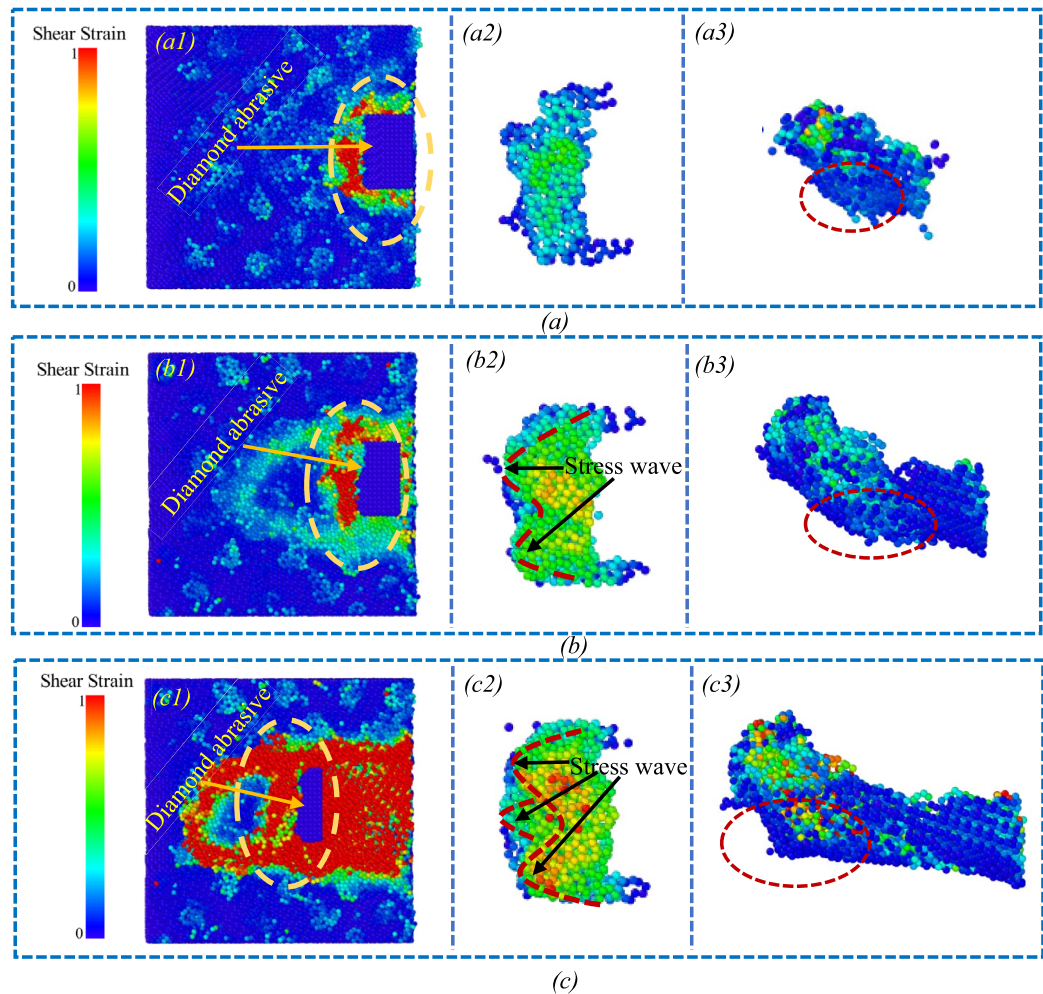
Figure 4. Cutting stress nematogram of rough polycrystalline 3C-SiC surface.

different at different depths and is therefore not purely based on the shape of the abrasive grain. From Fig. $4b_2$, it can be found the force shape of particles on the friction surface at this time presents two wave peaks, and the main force point is still under the slope of the abrasive particles. Figure $4b_3$ shows the traces left by the abrasive grain feed movement at 2.6 nm. The feed movement of the abrasive grains extrudes on the rough friction surface, resulting in the accumulation of some particles in front of the abrasive particles. The red dotted box shows the action of the bottom of the abrasive particle on the workpiece. The bottom of the workpiece receives less force than the front. Figure 4c shows the force cloud diagram when grinding to 5.6 *nm* and the force trace diagram of particles near the abrasive particles. In Fig. $4c_1$, it can be observed the force at the front end of the abrasive particles increases, and the surface force at the trace after grinding also increases. At the moment, the number of stressed atoms increases significantly, and the main stress point is still near the wave crest generated by abrasive particles. As can be seen in Fig. $4c_3$, the traces generated by abrasive particles increase significantly. The traces at the Angle are more obvious than those in the straight part, and more atoms are piled up. The shear force exerted by the abrasive grains on the polycrystalline 3C-SiC during the grinding process, especially in the shear stress range of 0.5–1 *nN*, leads to elastic stresses at the grain boundaries and inside the grains. This stress is unevenly distributed, especially at the grain boundaries, and easily induces crack initiation. Although the tangential force fluctuations are not significant, the non-uniform transfer of these forces and the wave-like force action pattern generate additional stresses in the grain contact region, contributing to brittle fracture at the grain boundaries.

Figure 5 shows the variation of friction force and related crystal structure during grinding of polycrystalline 3C-SiC with rough friction surface. Figure 5A shows the change of friction force when diamond abrasive grain grinding polycrystalline 3C-SiC rough friction surface position is 0–10 *nm*. In general, the friction force on the workpiece increases with the increase of grinding distance in the form of fluctuation. Figure 5C shows the atomic stress cloud at the corresponding position in Fig. 5A. Figure $5c_1$ shows the atomic stress image at 2 nm in Fig. 5A, the yellow dashed line represents the grain boundary. Figure $5(c_2)$, (c_3) and (c_4) respectively correspond to the atomic stress image at 4.4 *nm*, 6.4 *nm* and 8 *nm* in Fig. 5A. The part enclosed by the yellow dotted line is the part of the workpiece under the action of stress. At 2 nm, the friction in the Y and Z directions tends to increase, while the friction in the X direction tends to decrease. Figure $5c_1$ shows the grain boundaries
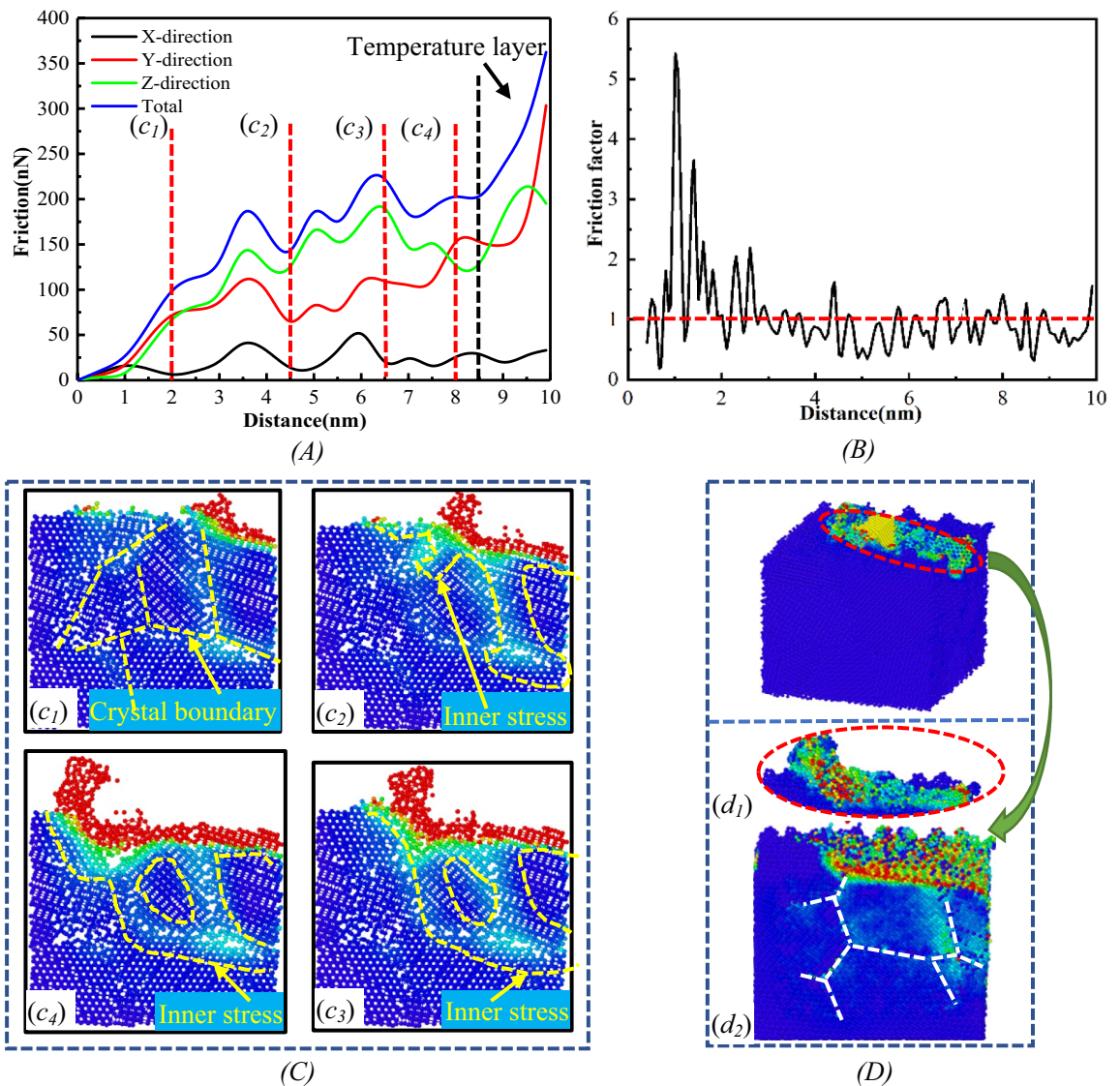
Figure 5. Variation of friction force in grinding process of polycrystalline 3C-SiC with rough surface.

are more susceptible to the forces in the presence of rough friction surfaces and abrasive particles. The force in the X direction plays a role in the removal of grain boundary sites. The force in the X direction is not the main driving force in the material removal mechanism, but it contributes to the removal of the material by interacting with forces in other directions. Combined with Fig. 5c_2, it is observed with the abrasive grains at the grain boundaries, the total friction peaks at 6.4 nm, as shown in Fig. 5c_3. At this time, the abrasive grains are grinding the polycrystalline grains, and the scope of the workpiece under the force extends forward to surround the grains. (c_4) is the atomic arrangement diagram of workpiece force at 8 *nm*, the force range varies forward with the feed movement of the abrasive grains. Figure 5B is a schematic diagram of the coefficient of friction during the friction process. The Fig. shows the adhesion of the abrasive grains to the contact surface of the workpiece is very tight, resulting in a friction coefficient greater than 1 and large fluctuations. At the same time, the contact tightness between the abrasive particles and the workpiece changes, resulting in large fluctuations in the coefficient of friction. Figure 5D shows the overall intention of workpiece processing at the position of 6.4 *nm*. Figure 5d_1 and (d_2) are the schematic diagram of the red dotted line in *(D)*. At this time, the abrasive particles are ground from the grain boundary to another grain part, and the friction force reaches a new peak, while the friction force in the X direction is decreasing. Since the polycrystalline friction surface structure is not as hard as the polycrystalline grains, the arrangement and stacking is more dispersed and easier to remove under force. The force on grain boundaries is more obvious than that on grain boundaries in polycrystals.

Analysis of the internal structure of polycrystalline silicon carbide nano-grinding

Figure 6 shows the variation of atomic arrangement and atomic stress maps at different positions during the grinding process on the rough friction surface of polycrystalline 3C-SiC. Figure 6A shows the variation of atomic arrangement during the grinding process with atomic arrangement maps at 8 nm, 6 nm, 4 nm and 2 nm. When
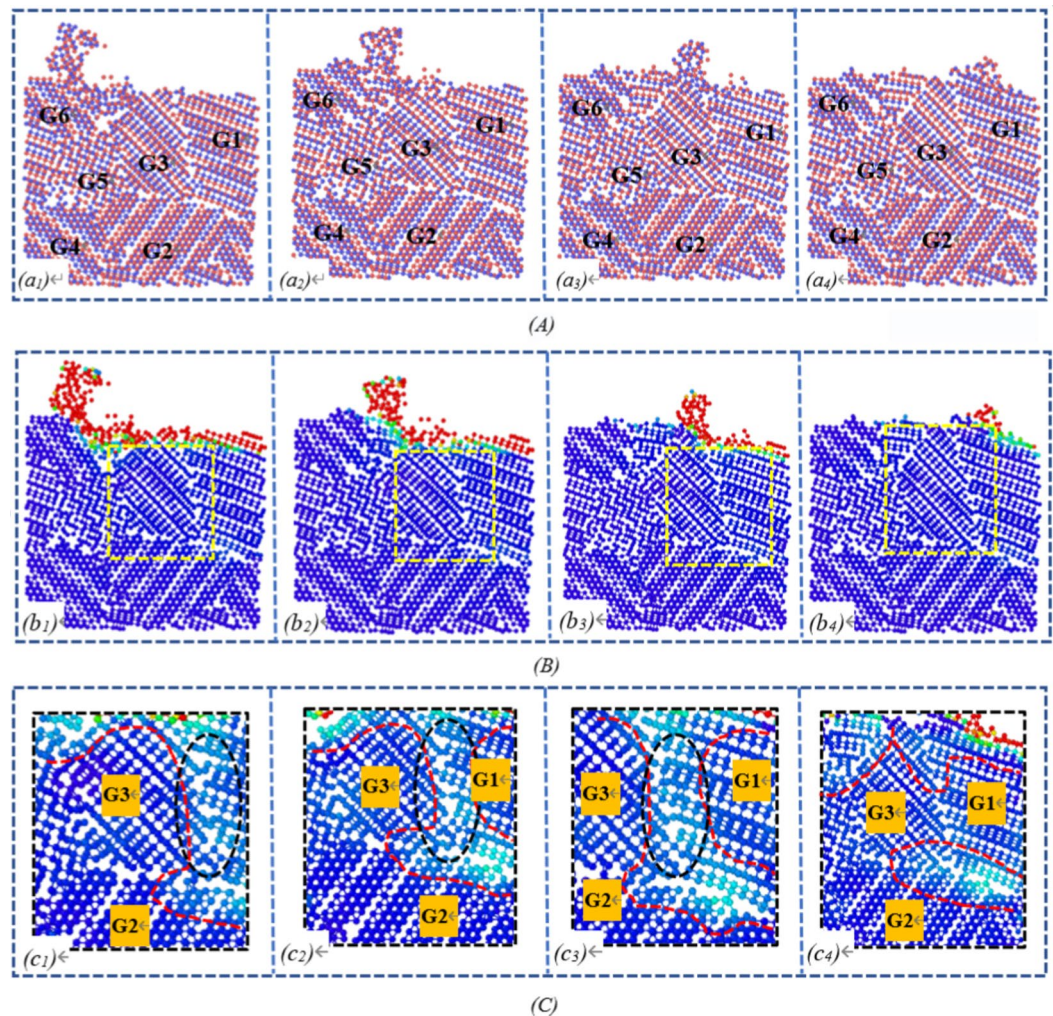
Figure 6. Atomic variation analysis diagram of polycrystalline 3C-SiC in grinding process.

diamond abrasive grains act on the rough friction surface, they mainly act on the three grains, G1, G3 and G6. The rough friction surface atoms under the action of abrasive particles lead to the covalent bond breaking in 3C-SiC and the formation of other new bonds, as well as generate new isolated discrete atoms. Figure 6B shows the stress image when the shear stress range is 0.5–1 *nN*. During the grinding process, the force generated by the abrasive particles on the rough friction surface of polycrystalline 3C-SiC concentrates on the grinding path and the inclined lower part of the abrasive particles. The red dotted line surrounds the force inside the workpiece. It is found that the stress is transferred inside the workpiece along the grain boundary. Firstly, local internal stress is generated at the grain boundary of G1 and G2, and the grain boundary of G1 and G3. The two internal stresses are transmitted and converged within the grain boundaries with the feed movement of the abrasive grains. In Fig. 6C the black dotted box shows the atomic state at the grain boundary during the grain feed movement. It is found that the atomic arrangement state at the grain boundary changes under the action of force, while the atomic arrangement state inside the crystal does not change.

Figure 7 shows the coordination analysis of polycrystalline 3C-SiC during the grinding process and the distribution of the force field strengths of the interaction potentials at different truncation distances. Figure 7A reveals the variation of the force field strengths of different interatomic interaction potentials with truncation distances. The C–C bonding force in diamond is dominant and the force field is mainly concentrated in the range of 1.5–5.5 units. Figure 7B further illustrates the distribution of the total force field strength with the truncation distance (radial distribution), peaks at a truncation distance of 2 unit lengths, then decreases as the truncation distance increases. Fig. 7C shows a schematic diagram of the atomic bond distribution of C–Si, Si–C, and Si–Si, Observeing the change of the C-Si bond of the red line. The corresponding findings are related to the strength of the stress field in Fig. 7B. This is the interaction between the abrasive particles and the workpiece during the friction process, the breaking of the C-Si atomic bonds, and the corresponding enhancement of the force field. Figure 7D shows the coordination analysis atom image at d = 8 nm. In Fig. 7D, the red particles are clearly concentrated near the diamond abrasive grains, clearly indicating the largest action potential and highest field strength near the diamond abrasive grains. The field intensity between grains is significantly higher than that at grain boundaries, while the interatomic interaction potential and field intensity at the edge of the workpiece and
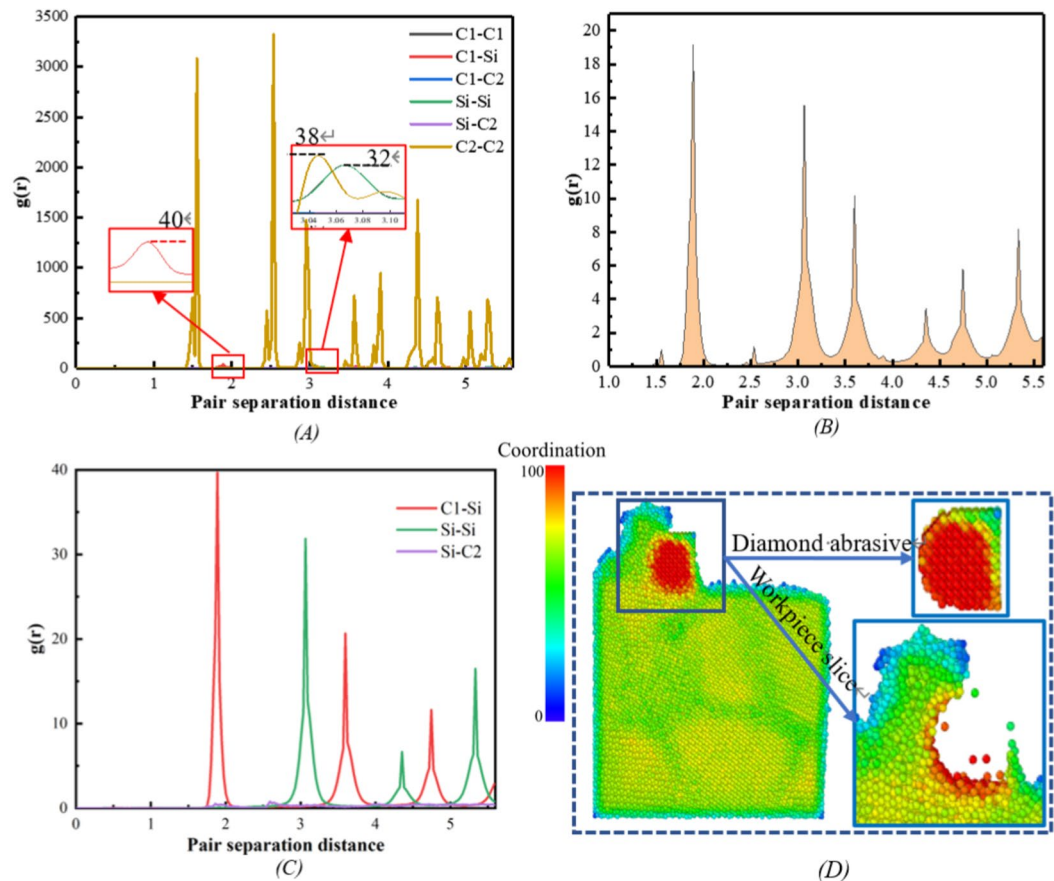
Figure 7. Coordination analysis of polycrystalline 3C-SiC in grinding process.

where the diamond is not in contact with the workpiece are relatively weak. During the grinding process, when the diamond abrasive grains are in contact with the 3C-SiC workpiece, a local high-pressure region is formed at the contact point because the hardness of the diamond abrasive grains is much higher than that of the 3C-SiC. During the movement of the diamond grits, tensile stresses are generated as the grits remove material from the workpiece during the cutting process, resulting in voids in the material behind the grits. In polycrystalline materials such as 3C-SiC, low strength is prevalent at grain boundaries and between grains, as well as there is a synergistic effect of high-pressure and tensile stresses exerted by diamond abrasive grains. It is easy to cause deformation of the workpiece material along grain boundaries or grain interfaces at the microscopic level, leading to frequent fracture along the grains.

Dislocation analysis of polycrystalline silicon carbide nano-grinding

Figure 8 shows the variation of the length and number of dislocations in the grinding process of polycrystalline 3C-SiC, as well as the generation, slip and conversion of dislocations. Figure 8a shows the change of the number of different types of dislocations along with the grinding time step, and Fig. 8b shows the change of the length of different types of dislocations along with the time step. The trend of the two images shows the number of similar dislocations is consistent with the change in the length of the dislocations. When the number of dislocations starts to increase, the length of the dislocation also increases. However, the number of dislocation and the growth rate of dislocation length are not consistent. For 15,000 to 40,000 time steps, the abrasive position is grinding and squeezing the grains, and the total number and length of dislocations maintains an increasing trend. However, at 44,000 time steps, the abrasive position transitions from grain to grain boundary and the trend in the total number of dislocations begins to decrease to a minimum. The $1/2 < 110 >$-type and $1/6 < 112 >$-type dislocations are the main dislocations in polycrystalline 3C-SiC during full grinding. Right view is an image of the right view of the defective surface using diamond grinding. Top view is an image of the top view of the defective surface when the workpiece is ground using diamond. Detail view is a partially enlarged image of the workpiece in the right view when it is ground in the misalignment line. As shown in Fig. 8c, the dislocation patterns at the 2 nm position under different viewing angles indicate the force exerted by the abrasive on the polycrystalline 3C-SiC grains during the feeding motion, resulting in the extrusion deformation between the grains. From the top view, the position marked with the blue frame line produces compression deformation. The dislocation view shows dislocations occurring primarily at the point of dislocation, including dislocation shedding and transformation centred on the extruded region. The red boxed line in the right view is a localised zoomed in detail view, the localised dislocations in the blue boxed line continue to exist while the different dislocations continue to
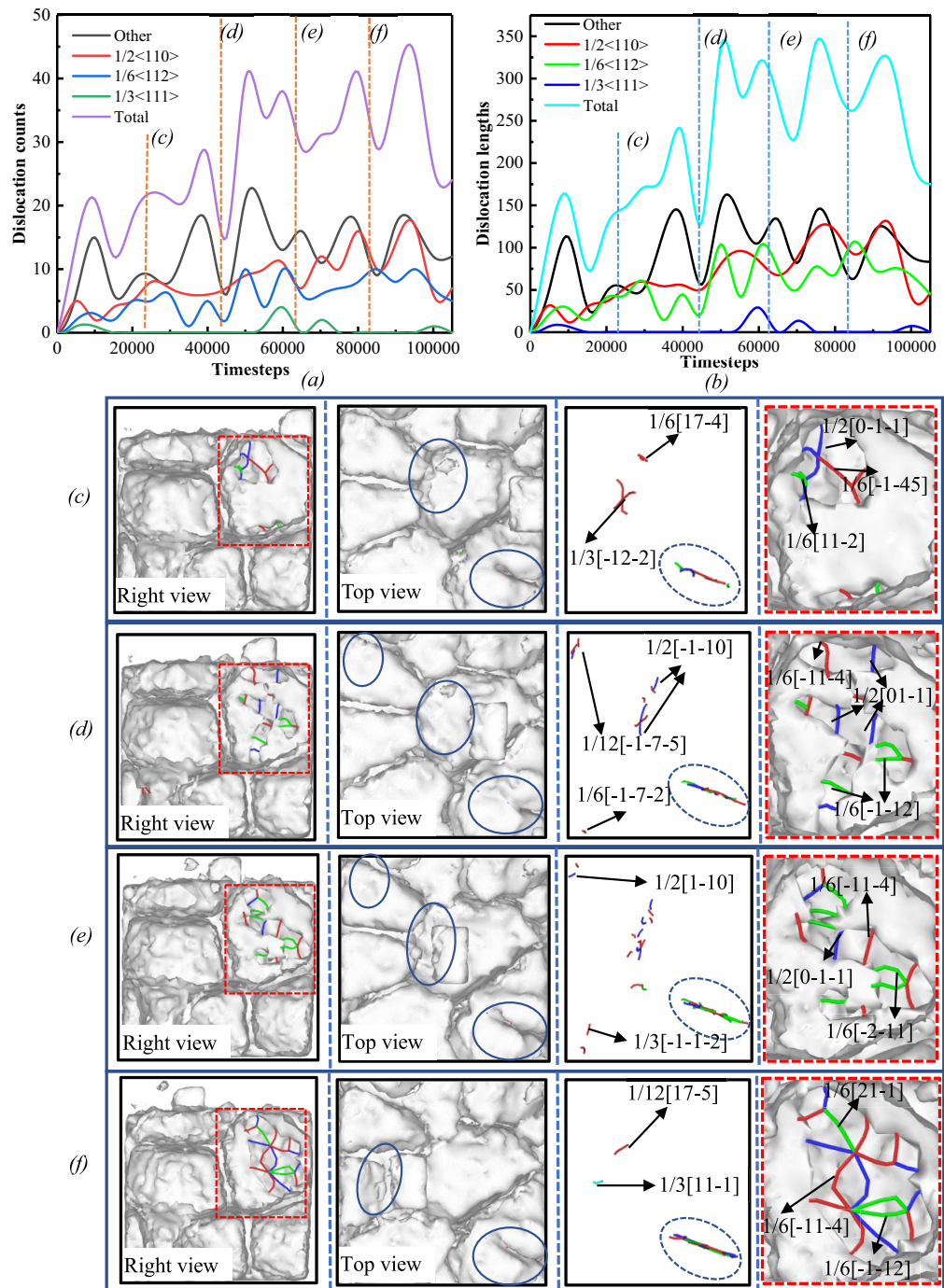
Figure 8. Generation, slip and conversion of dislocations in the grinding process of polycrystalline 3C-SiC.

transform. The activity of different types of dislocations (e.g. 1/2 < 110 >, 1/6 < 112 >, etc.) is related to the brittle fracture mode of the crystal, rather than being directed towards cutting faces that favour ductility. The ductility of a crystal is closely related to its structure, with specific faces and orientations exhibiting higher plasticity due to their atomic arrangement. For covalently bonded ceramic materials such as 3C-SiC, the ductility is usually low and the dislocation motion is mainly characterised by brittle fracture modes.

Conclusion

(1) Key features of the subsurface embrittlement mechanism of polycrystalline 3C-SiC rough friction surfaces during nano-grinding. The study found the interaction between the abrasive particles and the workpiece in the early stages of nano-grinding, especially in the 2.6 *nm* depth region, creates the phenomenon of " Stress concentration". Grain size is an important factor in determining the extent of subsurface damage,

and larger grains produce voids when fracturing at 8 nm, emphasising the moderating role of grain size in brittle fracture.

(2)   When grinding polycrystalline 3C-SiC, dislocation activity occurs intensively at grain boundaries, affecting material plasticity and energy dissipation. Friction varies with grinding depth and increases dramatically at d = 8.4 *nm*, reflecting the significant influence of the temperature layer on the grinding process. External forces cause intergranular extrusion to produce dislocations, with dislocations concentrating at grain boundaries and intersecting and fusing during the grinding process. This behaviour leads to plastic deformation of the friction surface being produced. Provides a scientific basis and theoretical guidance for the selection of grinding thickness of polycrystalline 3C-SiC with rough surfaces in practical machining applications.

Data availability

References

1.   Zhang, N.-L. *et al.* Preparation and characterization of lightweight SiC frameworks by connecting SiC fibers with SiC joints. *Ceram. Int.* **48**(6), 8751–8760 (2022).
2.   Tang, M. *et al.* Preparation and microstructure characterization of SiC/SiC joints reinforced by in-situ SiC nanowires. *Ceram. Int.* **46**(8), 12559–12565 (2020).
3.   Wang, H., Zhou, X., Peng, S., Zhang, H. & Zhou, X. Fabrication, microstructures and properties of SiCf/SiC composites prepared with two kinds of SiC fibers as reinforcements. *Carbon* **150**, 551 (2019).
4.   Chaika, A. N., Aristov, V. Y. & Molodtsova, O. V. Graphene on cubic-SiC. *Prog. Mater. Sci.* **89**, 1–30 (2017).
5.   Pacchioni, G. Spin qubits: Useful defects in silicon carbide. *Nat. Rev. Mater.* **2**(8), 17052 (2017).
6.   Wang, X. *et al.* Advances in modifications and high-temperature applications of silicon carbide ceramic matrix composites in aerospace: A focused review. *J. Eur. Ceram. Soc.* **41**(9), 4671–4688 (2021).
7.   Tan, T.-H. & Yan, J. Atomic-scale characterization of subsurface damage and structural changes of single-crystal silicon carbide subjected to electrical discharge machining. *Acta Mater.* **123**, 362–372 (2017).
8.   Barick, P., Jana, D. C. & Saha, B. P. Load-dependent indentation behavior of β-SiAlON and α-silicon carbide. *J. Adv. Ceram.* **2**(2), 185–192 (2013).
9.   Wu, H., Roberts, S. & Derby, B. Residual stress and subsurface damage in machined alumina and alumina/silicon carbide nano-composite ceramics. *Acta Mater.* **49**(3), 507–517 (2001).
10.   Agarwal, S. Optimizing machining parameters to combine high productivity with high surface integrity in grinding silicon carbide ceramics. *Ceram. Int.* **42**(5), 6244–6262 (2016).
11.   Agarwal, S. & Venkateswara Rao, P. Grinding characteristics, material removal and damage formation mechanisms in high removal rate grinding of silicon carbide. *Int. J. Mach. Tools Manuf.* **50**(12), 1077–1087 (2010).
12.   Rao, X., Zhang, F., Lu, Y., Luo, X. & Chen, F. Surface and subsurface damage of reaction-bonded silicon carbide induced by electrical discharge diamond grinding. *Int. J. Mach. Tools Manuf.* **154**, 103564 (2020).
13.   Wu, C., Li, B., Liu, Y. & Liang, S. Y. Surface roughness modeling for grinding of Silicon Carbide ceramics considering co-existence of brittleness and ductility. *Int. J. Mech. Sci.* **133**, 167–177 (2017).
14.   Esfe, M. H., Bahiraei, M. & Mir, A. Application of conventional and hybrid nanofluids in different machining processes: A critical review. *Adv. Coll. Interface Sci.* **282**, 102199 (2020).
15.   Eder, S. J., Cihak-Bayr, U., Bianchi, D., Feldbauer, G. & Betz, G. Thermostat influence on the structural development and material removal during abrasion of nanocrystalline ferrite. *ACS Appl. Mater. Interfaces* **9**(15), 13713–13725 (2017).
16.   Tian, Z. *et al.* Study on nanomechanical properties of 4H-SiC and 6H-SiC by molecular dynamics simulations. *Ceram. Int.* **45**, 21998–22006 (2019).
17.   Goel, S., Luo, X. & Reuben, R. L. Shear instability of nanocrystalline silicon carbide during nanometric cutting. *Appl. Phys. Lett.* https://doi.org/10.1063/1.4726036 (2012).
18.   Li, W. *et al.* Influence of the fiber orientation on 3D C/C–SiC composite material and its formation mechanism of the machining surface. *Int. J. Adv. Manuf. Technol.* **118**, 2725–2743 (2022).
19.   Liua, Y., Li, B., Chongjun, Wu., Kong, L. & Zheng, Y. Smoothed particle hydrodynamics simulation and experimental analysis of SiC ceramic grinding mechanism. *Ceram. Int.* **44**, 12194–12203 (2018).
20.   Goel, S. *et al.* Brittle–ductile transition during diamond turning of single crystal silicon carbide. *Int. J. Mach. Tools Manuf.* **65**, 15–21 (2013).
21.   Ranjitkar, S. *et al.* Surface-sensitive microwear texture analysis of attrition and erosion. *J. Dent. Res.* **96**(3), 300–307 (2016).
22.   Nazir, M. H., Khan, Z. A., Saeed, A., Siddaiah, A. & Menezes, P. L. Synergistic wear-corrosion analysis and modelling of nano-composite coatings. *Tribol. Int.* **121**, 30–44 (2018).
23.   Kim, Y.-C. *et al.* Indentation size effect in nanoporous gold. *Acta Mater.* **138**, 52–60 (2017).
24.   Kanematsu, D. *et al.* Observation of quantum size effect from silicon nanowall. *Nanoscale Res. Lett.* **11**(1), 530 (2016).
25.   Eswar Prasad, K. & Ramesh, K. T. Hardness and mechanical anisotropy of hexagonal SiC single crystal polytypes. *J. Alloy. Compd.* **770**, 158–165 (2019).
26.   Wenhu, Xu., Sheng, C. & Zhong, M. Effects of ultrasonic vibration on sapphire polishing investigated by molecular dynamics. *Tribol. Int.* **176**, 107911 (2022).
27.   Wang, S. *et al.* Monitoring of ductile–brittle transition mechanisms in sapphire ultra-precision grinding used small grit size grinding wheel through force and acoustic emission signals. *Measurement* **210**, 112557 (2023).
28.   Zheng, Z. *et al.* An analytical force and energy model for ductile-brittle transition in ultra-precision grinding of brittle materials. *Int. J. Mech. Sci.* **220**, 107107 (2022).
29.   Chen, R., Li, S., Wang, Z. & Xinchun, Lu. Mechanical model of single abrasive during chemical mechanical polishing: Molecular dynamics simulation. *Tribol. Int.* **133**, 40–46 (2019).
30.   Mirzaamiri, R., Akbarzadeh, S. & Ziaei-Rad, S. Molecular dynamics simulation and experimental investigation of tribological behavior of nanodiamonds in aqueous suspensions. *Tribol. Int.* **156**, 106838 (2021).
31.   Liu, B., Yang, H., Xu, Z., Wang, D. & Ji, H. Molecular dynamics simulation of nanomachining mechanism between monocrystalline and polycrystalline silicon carbide. *Adv. Theor. Simul.* **4**(8), 2100113 (2021).

32. Tersoff, J. Modeling solid state chemistry: InteratomicPotentials for multicomponent system. *Phys. Rev. B* **41**, 5566–5568 (1989).
33. Vashishta, P., Kalia, R. K. & Nakano, A. Multimillion atom molecular dynamics simulations of nanostructures on parallel computers. *J. Nanopart. Res.* **5**, 119–135 (2003).

Author contributions

Nanxing Wu and Xiang Ning devised the project, the main conceptual ideas, proof outline, and wrote the manuscript. Jiawen Huang and Jiao Li worked on all of the technical details and performed the numerical calculations for the suggested experiment. Dongliang Liu and Rumeng Zhang worked out the bound for quantum experiments and verified the results. All authors reviewed the manuscript.

Competing interests

The authors declare no competing interests.

Additional information

Correspondence and requests for materials should be addressed to N.W.

Reprints and permissions information is available at www.nature.com/reprints.

Publisher's note Springer Nature remains neutral with regard to jurisdictional claims in published maps and institutional affiliations.